J. Fluid Mech. (1983), *vol.* 131, *pp.* 251–269
Printed in Great Britain

The fluid dynamics of an attic space

By DIMOS POULIKAKOS AND ADRIAN BEJAN

Department of Mechanical Engineering, University of Colorado, Campus Box 427, Boulder, Colorado 80309

(Received 2 April 1982 and in revised form 9 November 1982)

This paper reports a fundamental study of the fluid dynamics inside a triangular (attic-shaped) enclosure with cold upper wall and warm horizontal bottom wall. The study was undertaken in three distinct parts. In the first part, the flow and temperature fields in the cavity are determined theoretically on the basis of an asymptotic analysis valid for shallow spaces ($H/L \to 0$, where H and L are the attic height and length). It is shown that in the $H/L \to 0$ limit the circulation consists of a single elongated cell driven by the cold upper wall. The net heat transfer in this limit is dominated by pure conduction. In the second part of the study, the transient behaviour of the attic fluid is examined, based on a scaling analysis. The transient phenomenon begins with the sudden cooling of the upper sloped wall. It is shown that both walls develop thermal and viscous layers whose thicknesses increase towards steady-state values. The criterion for the existence of distinct thermal layers in the steady state is $(H/L)^{\frac{1}{2}} Ra_H^{\frac{1}{4}} > 1$, where Ra_H is the Rayleigh number based on attic height. The corresponding criterion for distinct viscous wall jets is $(H/L)^{\frac{1}{2}} Ra_H^{\frac{1}{4}} Pr^{-\frac{1}{2}} > 1$, where Pr is the Prandtl number. The third phase of this study focused on a complete sequence of transient numerical simulations covering the ranges $H/L = 0.2,\ 0.4,\ 1$; $Ra_H/Pr = 10,\ 10^3,\ 10^5$; $Pr = 0.72,\ 6$. The numerical experiments verify the flow features described theoretically in the first two parts of the study. The effect of thermal convection on the net heat transfer between the bottom and top walls is illustrated numerically. Finally, the transient numerical experiments show that in the present parametric domain the single-cell circulation pattern is stable with respect to the Bénard instability expected in fluid layers heated from below.

1. Introduction

The objective of this article is to document the phenomenon of thermal convection through an attic or a wedge-shaped space, filled with a Newtonian fluid. The 'attic' geometry is a generic description for all trapezoidal enclosures whose upper and lower surfaces are not parallel.

The phenomenon of natural convection in spaces with perfectly parallel horizontal surfaces has received considerable attention because of its fundamental importance in geophysical fluid mechanics, solar-engineering applications, buildings and thermal-insulation systems (see e.g. Ostrach 1972; Catton 1979). The attic or wedge geometry is of equal importance in all these applications, yet the fluid mechanics of this geometry remains to be investigated. Two recent papers by Flack, Konopnicki & Rooke (1979) and Flack (1980) discuss for the first time the steady-state natural circulation in triangular enclosures filled with air, in the range $7.5 \times 10^4 < Ra_H < 10^6$. The results reported in these papers are all experimental and, as pointed out by

Flack *et al.* (1979), analytical or numerical studies on the same subject are not available. Most recently, Bejan & Poulikakos (1982) studied analytically the natural convection in a wedge-shaped porous layer cooled from above, and showed that the flow pattern can differ fundamentally from the Bénard circulation encountered in constant-thickness horizontal layers. It is important to establish whether the same fundamental departure from the Bénard flow occurs in an attic-shaped enclosure filled only with Newtonian fluid.

In the context of an attic, we can identify two basic sets of temperature boundary conditions: (*a*) daytime (warm top and cold bottom), when the fluid in the enclosure is stably stratified in the steady state; and (*b*) night-time (cold top and warm bottom), when the steady circulation of fluid is possible. The present study focuses on 'night-time' temperature conditions and seeks to establish the damaging effect posed by the fluid circulation on the thermal-insulation potential of the fluid layer which fills the cavity.

2. Mathematical formulation

Consider the two-dimensional cavity shown schematically in figure 1. The two surfaces that are active, i.e. those surfaces that fuel the circulation of fluid in the cavity, are at different temperatures ($T_C < T_H$) and form an angle θ. The height/length aspect ratio of the enclosure is $A = H/L$. In order to model the operation during nighttime conditions, the warm surface (T_H) is chosen as horizontal. It is worth noting, however, that if the angle θ is small the conclusions of this study apply just as well to the case where the cold surface is horizontal and the warm surface is of slope $-\theta$; this alternative geometry may be regarded as a simple two-dimensional model for the near-shore thermal circulation in a shallow lake with sloping bottom.

The equations governing the conservation of mass, momentum and energy at every point in the enclosure are

$$\frac{\partial u_*}{\partial x_*}+\frac{\partial v_*}{\partial y_*}=0, \tag{1}$$

$$\frac{\partial u_*}{\partial t_*}+u_*\frac{\partial u_*}{\partial x_*}+v_*\frac{\partial u_*}{\partial y_*}=-\frac{1}{\rho_0}\frac{\partial P_*}{\partial x_*}+\nu\nabla^2 u_*, \tag{2}$$

$$\frac{\partial v_*}{\partial t_*}+u_*\frac{\partial v_*}{\partial x_*}+v_*\frac{\partial v_*}{\partial y_*}=-\frac{1}{\rho_0}\frac{\partial P_*}{\partial y_*}+\nu\nabla^2 v_*-\frac{\rho g}{\rho_0}, \tag{3}$$

$$\frac{\partial T_*}{\partial t_*}+u\frac{\partial T_*}{\partial x_*}+v\frac{\partial T_*}{\partial y_*}=\alpha\nabla^2 T_*, \tag{4}$$

with the following boundary conditions:

$$\begin{aligned} &u_*=v_*=0 \quad \text{on all solid boundaries,}\\ &T_*=T_C, T_H \quad \text{on the top and bottom walls respectively,}\\ &u_*=0,\ \frac{\partial T_*}{\partial x_*}=0 \quad \text{in the plane of symmetry } (x_*=L). \end{aligned} \tag{5}$$

In these equations, u_*, v_* are the horizontal and vertical velocity components, x_*, y_* the coordinates of each point, and P_*, T_* the fluid pressure and temperature. Properties ν, ρ_0, β and α represent the kinematic viscosity, fluid density, coefficient of thermal expansion and thermal diffusivity respectively. All properties are referred

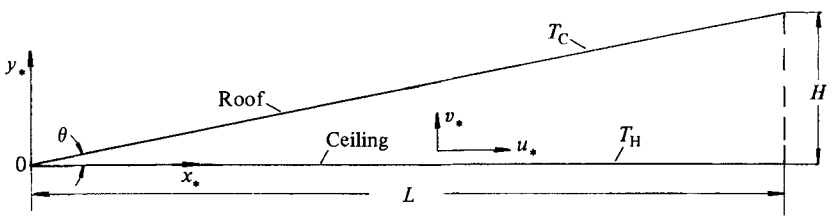

FIGURE 1. Schematic of a shallow attic space filled with Newtonian fluid.

to a characteristic reference temperature of the fluid, T_0. For moderate temperature differences as encountered in real attics, solar collectors and shallow reservoirs, the Boussinesq approximation is appropriate:

$$\rho \approx \rho_0[1-\beta(T-T_0)]. \tag{6}$$

Combining this statement with (2) and (3) and eliminating the pressure P_* leads to a single momentum-conservation statement,

$$\frac{\partial}{\partial t_*}\left(\frac{\partial u_*}{\partial y_*}-\frac{\partial v_*}{\partial x_*}\right)+\frac{\partial}{\partial y_*}\left(u_*\frac{\partial u_*}{\partial x_*}+v_*\frac{\partial u_*}{\partial y_*}\right)-\frac{\partial}{\partial x_*}\left(u_*\frac{\partial v_*}{\partial x_*}+v_*\frac{\partial v_*}{\partial y_*}\right)$$
$$=\nu\frac{\partial^3 u_*}{\partial y_*^3}-\frac{\partial^3 v_*}{\partial x_*\partial y_*^2}-g\beta\frac{\partial T_*}{\partial x_*}. \tag{7}$$

It is known that whenever a rectangular enclosure is heated from below the fluid in it may develop thermal instabilities of the Bénard type (Bénard 1901; Rayleigh 1916; Chandrasekhar 1961). However, in the case of an attic space in winter conditions the inclination of the roof will tend to generate a single (primary) cell, which will sweep the entire length of the roof, much in the manner of the elongated counterflow in a shallow horizontal fluid layer heated in the end-to-end direction (Cormack, Leal & Imberger 1974). In view of these two possibilities, the Bénard flow and the one-cell counterflow, it is not *a priori* clear which type of flow will exist in the cavity. To shed light on this question, we first rely on an asymptotic theory of the type available for porous layers (Bejan & Poulikakos 1982), to determine the flow in very shallow attic spaces.

3. Asymptotic theory for the steady state

In the limit $A = H/L \to 0$, the steady-state part of the problem formulated in §2 lends itself to an asymptotic solution of the type developed by Cormack *et al.* (1974) for shallow fluid layers, and by Walker & Homsy (1978) for shallow porous layers. We note that $O(x_*) = L$ and $O(y_*) = H$, hence, from (7), $O(u_*) = g\beta H^3\Delta T/\nu L$, where $\Delta T = T_H - T_C$. Based on this scaling, the governing equations are written in dimensionless form as

$$Gr_H A^2\left\{\frac{\partial}{\partial y}\left(\frac{\partial\Psi}{\partial y}\frac{\partial^2\Psi}{\partial x\partial y}-\frac{\partial\Psi}{\partial x}\frac{\partial^2\Psi}{\partial y^2}\right)-A^2\frac{\partial}{\partial x}\left(\frac{\partial\Psi}{\partial x}\frac{\partial^2\Psi}{\partial x\partial y}-\frac{\partial\Psi}{\partial y}\frac{\partial^2\Psi}{\partial x^2}\right)\right\}$$
$$=\frac{\partial}{\partial y}\left(A^2\frac{\partial^3\Psi}{\partial x\partial y^2}+\frac{\partial^3\Psi}{\partial y^3}\right)+A^2\frac{\partial}{\partial x}\left(A^2\frac{\partial^3\Psi}{\partial x^3}+\frac{\partial^3\Psi}{\partial x\partial y^2}\right)-\frac{\partial T}{\partial x}, \tag{8}$$

$$Gr_H Pr\, A^2\left(\frac{\partial\Psi}{\partial y}\frac{\partial T}{\partial x}-\frac{\partial\Psi}{\partial x}\frac{\partial T}{\partial y}\right)=A^2\frac{\partial^2 T}{\partial x^2}+\frac{\partial^2 T}{\partial y^2}, \tag{9}$$

with the following notation:

$$x = \frac{x_*}{L}, \quad y = \frac{y_*}{H}, \quad \Psi = \frac{\Psi_*}{g\beta H^4 \Delta T/\nu L}, \quad T = \frac{T-T_C}{T_H-T_C}, \quad u_* = \frac{\partial \Psi_*}{\partial y_*}, \quad v_* = -\frac{\partial \Psi_*}{\partial x_*}. \tag{10}$$

In (8) and (9) Pr and Gr_H are the Prandtl number ν/α and the Grashof number

$$Gr_H = \frac{g\beta(T_H - T_C)H^3}{\nu^2}. \tag{11}$$

Noting that the small parameter $A = H/L$ appears as A^2 in (8) and (9), we seek series solutions of the type

$$\left.\begin{aligned} \Psi(x,y) &= \Psi_0(x,y) + A^2\Psi_2(x,y) + A^4\Psi_4(x,y) + \ldots, \\ T(x,y) &= T_0(x,y) + A^2 T_2(x,y) + A^4 T_4(x,y) + \ldots \end{aligned}\right\} \tag{12}$$

that satisfy the boundary conditions

$$\left.\begin{aligned} T = 1, \quad \Psi = 0, \quad \frac{\partial \Psi}{\partial y} = 0 \quad (y = 0), \\ T = 0, \quad \Psi = 0, \quad \frac{\partial \Psi}{\partial y} = 0 \quad (y = f(x)). \end{aligned}\right\} \tag{13}$$

Here $f(x)$ is a smooth function of x which describes the shape of the upper wall of the attic space. If, as in figure 1, the upper wall is flat then the roof-shape function has the simple form $f(x) = x$. It is shown later in this section that the roof shape influences the circulation pattern in the enclosure.

The successive terms in the series solution (12) are derived systematically by combining (12) with (8), (9) and (13). For brevity, and since the analytical procedure is described in detail in Cormack *et al.* (1974), Walker & Homsy (1978) and Bejan & Poulikakos (1982), we list the final expressions obtained for the $O(A^0)$ and $O(A^2)$ terms:

$$T_0 = 1 - \frac{y}{f}, \tag{14}$$

$$\psi_0 = \frac{1}{120}\frac{f'}{f^2}y^5 - \frac{1}{40}f'y^3 + \frac{1}{60}ff'y^2, \tag{15}$$

$$T_2 = C_1 y^7 + C_2 y^5 + C_3 y^4 + C_4 y^3 + C_5 y, \tag{16}$$

$$\psi_2 = a_1 y^{11} + a_2 y^9 + a_3 y^8 + a_4 y^7 + a_5 y^6 + a_6 y^5 + a_7 y^4 + a_8 y^3 + a_9 y^2. \tag{17}$$

The analytical expressions for coefficiency C_i and a_i are given as (A 1) and (A 2) in the appendix.

The analytic result presented in (14)–(17) is of considerable generality. Once the upper wall shape function is defined, (14)–(17) provide a two-term approximate solution for the steady-state temperature and flow fields in the enclosure. To illustrate, we choose the simple case of the shallow triangular shape shown in figure 1, $f(x) = x$. In this case, (14) and (15) reduce to

$$T_0 = 1 - \frac{y}{x}, \tag{18}$$

$$\psi_0 = \frac{1}{120}\frac{y^5}{x^2} - \frac{y^3}{40} + \frac{1}{60}xy^2. \tag{19}$$

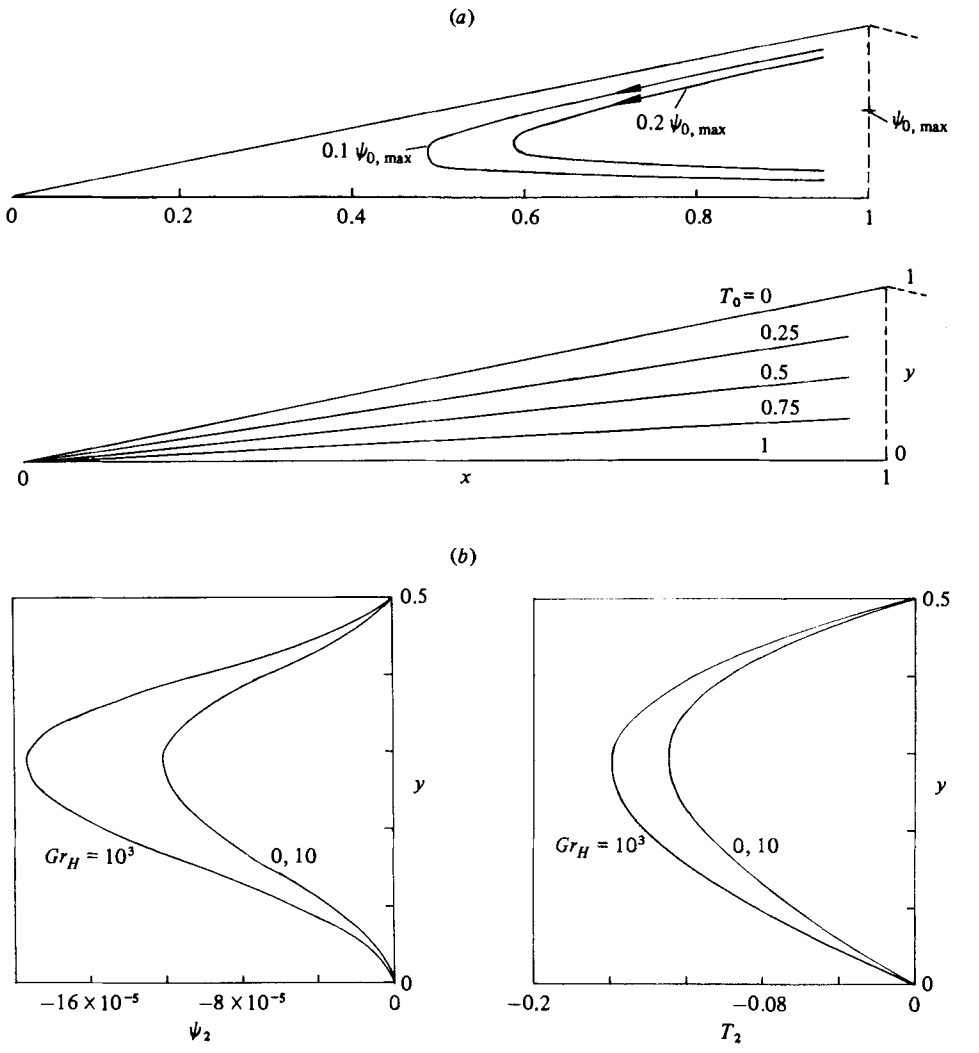

FIGURE 2. (*a*) Streamlines and isotherms corresponding to the zeroth-order asymptotic solution. (*b*) Second-order stream-function and temperature profiles at $x_* = \frac{1}{2}L$; the fluid is air ($Pr = 0.72$).

The resulting expressions for the numerical coefficients of T_2 and ψ_2 in (16) and (17) are listed as (A 3) and (A 4) in the appendix.

Figure 2(*a*) shows the patterns of streamlines and isotherms corresponding to the $O(A^0)$ solution. The slight tilt in the isotherms gives rise to a steady counterclockwise motion with a gyration timescale of order $L/u_* \approx L^2/\nu Gr_H$. The $O(A^2)$ terms of this limiting solution are plotted in figure 2(*b*) as stream-function and temperature profiles at $x = 0.5$. It is worth noting that the $O(A^2)$ correction (ψ_2, T_2) is not proportional to the Grashof number Gr_H, unlike the $O(A^2)$ correction for the parallel core flow of shallow rectangular cavities (Cormack *et al.* 1974).

Regarding the streamline pattern of figure 2(*a*), it is important to keep in mind that this pattern exists only in the limit $A \to 0$, and that for the sake of clarity only, the figure 2(*a*) shows an exaggerated angle. Not visible on figure 2(*a*) is the end-turn region (near $x = 1$), which is infinitely short (of order A). The right end region serves to turn the flow by 180°, and assuming that the $x_* = L$ plane is adiabatic has no effect

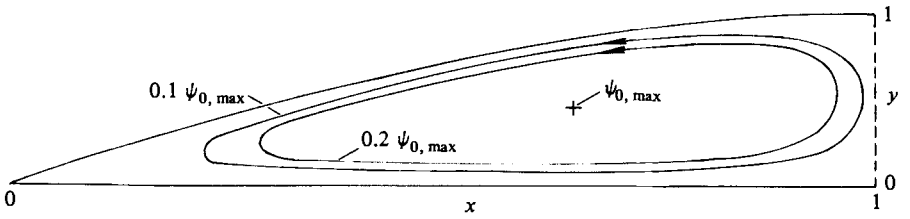

FIGURE 3. Zeroth-order flow pattern under a smooth roof, $f(x) = \sin\frac{1}{2}\pi x$.

on either the intensity of the counterclockwise cell or the enthalpy carried by it. Equations (18) and (19) describe the flow and temperature only in the wedge region, where the assumed scaling applies; the same equations do not apply near $x_* = L$, where both y_* and x_* are of order H.

The pattern in a symmetric (A-shaped) attic space consists of piecing together, end-to-end, two asymptotically shallow patterns of the type shown in figure 2(*a*). Thus a symmetric attic will contain two identical cells, the left counterclockwise and the right clockwise, which merge in the middle to form a localized (narrow) updraft right under the peak of the roof. If the roof changes slope from A to $-A$ smoothly (not abruptly as in an A-frame space) then the updraft will no longer be localized; instead, it will be distributed over a middle region which scales with L. To illustrate this, consider the circulation under a smooth symmetric roof described by $f(x) = \sin\frac{1}{2}\pi x$. The corresponding limiting forms of T and ψ are

$$T_0 = 1 - \frac{y}{\sin\frac{1}{2}\pi x}, \tag{20}$$

$$\Psi_0 = \frac{1}{40}\pi\cos\tfrac{1}{2}\pi x\left\{\frac{1}{6}\frac{y^5}{\sin^2\frac{1}{2}\pi x} - \frac{1}{2}y^3 + \frac{1}{3}y^2\sin\tfrac{1}{2}\pi x\right\}. \tag{21}$$

Figure 3 shows the cellular flow pattern and the fact that the left end-turn region now occupies approximately one-third of the attic length.

Regarding the heat transfer between the two walls, the isotherms of figure 2(*a*) indicate that in the limit $H/L \to 0$ conduction is the prevailing mechanism. There is, however, an incipient convective effort which can be calculated from the heat flux along either surface. The Nusselt number is defined as

$$Nu = \frac{\text{net heat transfer}}{kL\Delta T/H} = -\int_{0+}^{1}\left(\frac{\partial T}{\partial y}\right)_{y=0}\mathrm{d}x$$

$$= \left(1 + \frac{A^2}{3} + \ldots\right)\int_{0+}^{1}\frac{\mathrm{d}x}{x} + \frac{17A^2Gr_HPr}{50\,400} + \ldots. \tag{22}$$

The first term on the right-hand side is the contribution due to pure conduction between floor and ceiling: this term blows up if the two surfaces (T_H, T_C) indeed make direct contact at the tip ($x = 0$) (Arpaci 1966). In reality, the wall region of length δ near the tip of a shallow wedge (figure 1) will always reach an average temperature between T_H and T_C, hence the corner region will not contribute appreciably to the heat transfer across the attic space. The result (22) proves that, relative to pure conduction, the first convective contribution to the heat-transfer rate scales as the group A^2Gr_HPr, unlike in the case of shallow constant-thickness layers heated in the horizontal direction, where it scales as the group $A^2Gr_H^2Pr^2$ (Cormack *et al.* 1974).

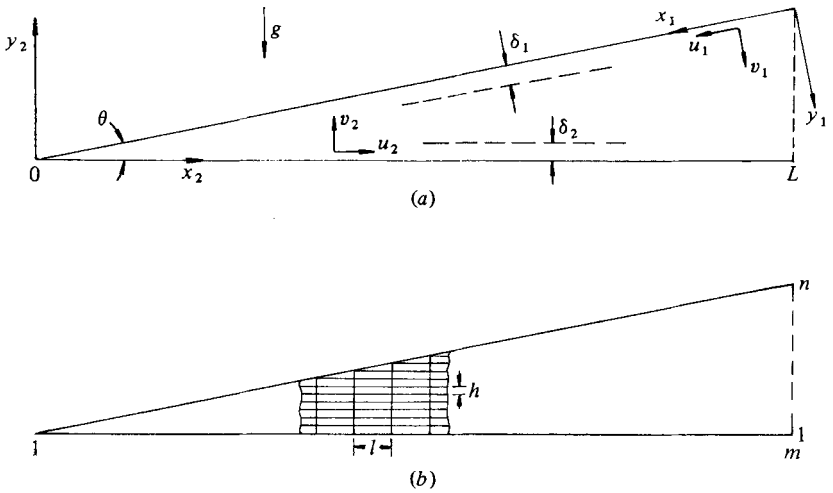

FIGURE 4. (*a*) Schematic of the boundary layers developing along the top and bottom walls. (*b*) Schematic of the grid used for the numerical solution.

4. Scale analysis of the transient regime

We gain further insight into the fluid dynamics of the attic space by focusing on its transient response to sudden changes in temperature along the two walls. The transient behaviour of an attic space is relevant in itself, considering that many real-life systems are designed to function under time-varying conditions (witness in this regard the daily cycle imposed on attics and fluid-filled cavities in solar collectors). However, a theoretical understanding of the transient behaviour of the enclosure is most valuable in a fundamental sense: as shown by Patterson & Imberger (1980) the proper identification of the timescales of various flow features that develop inside the cavity makes it possible to predict theoretically the basic flow features that will survive in the steady state.

In what follows we rely on pure scaling arguments to describe the main features of the flow in an isothermal attic fluid subjected to sudden cooling along its tilted wall, while the horizontal wall is kept at the initial temperature (figure 4*a*).

4.1. *The growth of a boundary layer along the top wall*

Consider the triangular enclosure shown in figure 4(*a*), where the coordinate system (x_1, y_1) is attached to the top wall. What triggers the transient natural convection phenomenon is the temperature difference ΔT instantly applied across the attic space by suddenly cooling the roof. The energy equation (4) indicates that since the fluid is initially motionless the top-wall cooling effect will first propagate into the fluid layer through pure conduction. As shown in figure 4(*a*) the top wall develops a thermal layer whose thickness δ_1 initially grows as

$$\delta_1 \approx (\alpha t)^{\frac{1}{2}}. \tag{23}$$

This result follows from (4), which immediately after $t = 0$, expresses a balance between the thermal-inertia term and the y_1 diffusion term.

The momentum equation (7), written in the $(x_1, y_1; u_1, v_1)$-system of the top wall, indicates that the unsteady inertia term is of order $u_1/t\delta_1$, while the viscous term is of order $\nu u_1/\delta_1^3$; the ratio of unsteady inertia to viscous diffusion is therefore $O(Pr^{-1})$.

Hence the correct force balance for Prandtl numbers of order one or greater is between buoyancy and viscous diffusion which, assuming that the thermal layer δ_1 is slender ($\delta_1 < L$), yields the velocity scale

$$u_1 \approx \frac{g\beta\Delta TA}{Pr}t. \tag{24}$$

Note that for the objectives of the present scaling analysis, we have assumed that $\sin\theta \approx \theta \approx A$ and $\cos\theta \approx 1$.

As time passes, the boundary-layer thickness δ_1 continues to grow until the heat transfer from the fluid layer to the wall is balanced by the energy convected into the top-wall region by the fluid sinking through the layer. At this point the energy equation (4) expresses a balance between convection and diffusion in the y_1 direction,

$$u_1\frac{\Delta T}{L} \approx \alpha\frac{\Delta T}{\delta_1^2}. \tag{25}$$

Using the boundary-layer thickness scale (23) and the velocity scale (24), we conclude that the growth of the boundary layer along the top wall ends at a time of order

$$t_{1f} \approx Ra_H^{-\frac{1}{2}}\frac{H^2}{A\alpha}. \tag{26}$$

where Ra_H is the Rayleigh number $PrGr_H$. Therefore the final thickness of the boundary layer along the top wall is

$$\delta_{1f} \approx Ra_H^{-\frac{1}{4}}A^{-\frac{1}{2}}H. \tag{27}$$

It is worth stressing that the energy balance (25) between conduction and convection implies that the thermal-inertia term $\partial T/\partial t$ has become negligible, in other words, the top-wall boundary layer has reached steady state. At this stage the u_1 velocity scale is

$$u_{1f} \approx Ra_H^{\frac{1}{4}}\frac{\alpha}{H}. \tag{28}$$

The final thickness (27) of the top-wall thermal boundary layer, can be compared with the vertical dimension of the cavity. The thermal boundary layer along the upper wall will be distinct when $\delta_{1f} < H$, i.e. when

$$Ra_H^{\frac{1}{4}}A^{\frac{1}{2}} > 1. \tag{29}$$

The criterion (29) can also be derived on the basis of a time comparison. The two characteristic times of interest are the time marking the end of layer growth (t_{1f}, (26)) and the diffusion time across the enclosure, H^2/α. A distinct boundary layer will exist only if it becomes convective before the heat can be transferred by conduction from the bottom to the top of the cavity, i.e. when

$$t_{1f} < \frac{H^2}{\alpha}. \tag{30}$$

Combining this condition with (26) leads once again to (29).

Finally, it is worth keeping in mind that the length- and timescales discussed above follow from the assumption that, immediately before reaching its terminal thickness δ_{1f}, the boundary layer along the top wall is slender ($\delta_{1f} < H$). This assumption was made in the discussion which preceded (24). Using (27), the slenderness condition

$\delta_{1f} < L$ translates into

$$Ra_H^{\frac{1}{4}} A^{\frac{1}{2}} > 1, \tag{31}$$

which is identical to (29).

Concurrently with the formation of a thermal boundary layer, the diffusion of vorticity into the attic space generates a viscous boundary layer. The thickness δ_1' of this viscous layer is a direct result of a balance between the viscous and inertia terms in the momentum equation,

$$\delta_1' \approx (\nu t)^{\frac{1}{2}}. \tag{32}$$

When the thermal layer has reached the steady state, the viscous layer has a thickness of order

$$\delta_{1f}' \approx Ra_H^{-\frac{1}{4}} Pr^{\frac{1}{2}} \frac{H}{A^{\frac{1}{2}}}. \tag{33}$$

Hence the timescale (26) represents the steady state for a double boundary layer on the top wall; a thermal layer governed by a viscous–buoyancy balance against the wall, surrounded by an outer viscous layer governed by a viscous–inertia balance. Finally, the presence of a distinct viscous boundary layer along the top wall means $\delta_{1f} < H$, in other words

$$Pr^{-\frac{1}{2}} Ra_H^{\frac{1}{4}} A^{\frac{1}{2}} > 1. \tag{34}$$

4.2. *The discharge from the top-wall layers and the development of horizontal layers along the bottom wall*

Focusing once again on the beginning of time ($t = 0^+$), the cold tilted wall drives downward a stream of thickness $\delta_1(t)$ and velocity $u_1 \approx (g\beta\Delta T A/Pr)\, t$, (24). This stream is colder than the rest of the fluid in the enclosure, and, as a result, after reaching the $x_2 = 0$ corner of the wedge, it has no choice but to move horizontally to the right along the bottom wall (figure 4*a*). Invoking the principle of mass convection, the volumetric flow rate of the horizontal stream, $u_2\delta_2$, is the same as $u_1\delta_1$, namely

$$u_2\delta_2 \approx \frac{g\beta\Delta T A}{Pr} \alpha^{\frac{1}{2}} t^{\frac{3}{2}}. \tag{35}$$

Some time before the steady state is reached, the flow in the vicinity of the bottom wall is described by a balance between friction and buoyancy forces

$$\frac{\nu u_2}{\delta_2^3} \approx g\beta \frac{\Delta T}{L}. \tag{36}$$

Combining this statement with (35) yields the short timescales for the velocity and the thickness of the horizontal intrusion layer

$$u_2 \approx H^{\frac{1}{4}} \alpha^{\frac{3}{8}} t^{\frac{3}{8}}, \tag{37}$$

$$\delta_2 \approx \frac{g\beta\Delta T}{\nu H^{\frac{1}{4}}} A \alpha^{\frac{2}{8}} t^{\frac{2}{8}}. \tag{38}$$

The end of the development of the bottom-wall layer is marked by a conduction convection balance in the energy equation (4):

$$\frac{u_2}{L} \approx \frac{\alpha}{\delta_2^2}. \tag{39}$$

The group of equations (37)–(39) defines the following time, velocity and thickness

scales for the bottom intrusion layer in the steady state:

$$t_{2f} \approx Ra_H^{-\frac{8}{15}} A^{-\frac{14}{15}} \frac{H^2}{\alpha}, \tag{40}$$

$$u_{2f} \approx \frac{\alpha}{H} Ra_H^{\frac{2}{5}} A^{-\frac{1}{5}}, \tag{41}$$

$$\delta_{2f} \approx HRa_H^{-\frac{1}{5}} A^{-\frac{2}{5}}. \tag{42}$$

Comparing the new timescale t_{2f} with the time required by the top-wall layer to reach the steady state t_{1f}, (26), we conclude that the bottom-wall layer will develop faster than the top-wall layer if

$$\frac{t_{2f}}{t_{1f}} < 1 \quad \text{or} \quad Ra_H^{\frac{1}{4}} A^{\frac{1}{2}} > 1. \tag{43}$$

The criterion (43) is identical with (29), which is necessary for the existence of a thermal boundary layer along the top wall. Hence, when they exist, the two layers develop simultaneously and the top layer reaches steady state after the bottom layer, Comparing the final thickness δ_{2f} of the horizontal intrusion layer with the height of the enclosure H yields the necessary condition for the existence of a distinct, thermal layer along the bottom wall:

$$A^{\frac{1}{2}} Ra_H^{\frac{1}{4}} > 1. \tag{44}$$

Note that this result is identical with (29).

In the steady state, the bottom-wall thermal layer is surrounded by a viscous layer ruled by a balance between inertia and viscous diffusion in (7): the thickness of this layer is

$$\delta'_{2f} \approx Ra_H^{-\frac{1}{4}} Pr^{\frac{1}{2}} \frac{H}{A^{\frac{1}{2}}}, \tag{45}$$

which is identical with the thickness scale for the viscous layer forming along the wall. Thus the criterion for the existence of a distinct viscous layer along the bottom wall is the same as the criterion (34) for the top wall.

5. Numerical experiments

The flow features discussed theoretically in §§3 and 4 were verified on the basis of a complete series of numerical simulations. It was assumed that the fluid contained in the attic space is originally motionless and of a uniform temperature T_H; as in the transient scale analysis of §4 the cavity is suddenly cooled from the top by decreasing the temperature of the sloping wall (the roof). Throughout this experiment, the temperature of the horizontal wall is maintained at the initial level T_H.

The numerical solution is aided somewhat by introducing the stream function, (10), and the vorticity function defined as

$$w_* = -\left(\frac{\partial^2 \psi_*}{\partial x_*^2} + \frac{\partial^2 \psi_*}{\partial y_*^2}\right). \tag{46}$$

Taking H, ν/H and $\Delta T = T_H - T_C$ as reference units for length, velocity and temperature variation, we define the new dimensionless variables

$$x = \frac{x_*}{H}, \quad y = \frac{y_*}{H}, \quad t = \frac{t_*}{H^2/\nu}, \quad u = \frac{u_*}{\nu/H}, \tag{47}$$

$$v = \frac{v_*}{\nu/H}, \quad \psi = \frac{\psi_*}{\nu}, \quad w = \frac{w_*}{\nu/H^2}, \quad T = \frac{T_* - T_C}{T_H - T_C}. \tag{48}$$

The corresponding dimensionless forms of the governing equations and boundary conditions are

$$u = \frac{\partial \psi}{\partial y}, \quad v = -\frac{\partial \psi}{\partial x}, \tag{49), (50}$$

$$w = -\left(\frac{\partial^2}{\partial x^2} + \frac{\partial^2}{\partial y^2}\right)\psi, \tag{51}$$

$$\frac{\partial w}{\partial t} + \frac{\partial (uw)}{\partial x} + \frac{\partial (vw)}{\partial y} = Gr_H \frac{\partial T}{\partial x} + \frac{\partial^2 w}{\partial x^2} + \frac{\partial^2 w}{\partial y^2}, \tag{52}$$

$$\frac{\partial T}{\partial t} + \frac{\partial (uT)}{\partial x} + \frac{\partial (vT)}{\partial y} = \frac{1}{Pr}\left(\frac{\partial^2 T}{\partial x^2} + \frac{\partial^2 T}{\partial y^2}\right), \tag{53}$$

$$\left.\begin{aligned} &u = v = 0, \quad \psi = 0, \quad T = 1 \quad (y = 0), \\ &u = 0 \quad \psi = 0, \quad w = 0, \quad \frac{\partial T}{\partial x} = 0 \quad (x = A^{-1}\text{: the centre of symmetry of the attic}), \\ &u = v = 0, \quad \psi = 0, \quad T = 0 \quad (y = Ax). \end{aligned}\right\} \tag{54}$$

The effect of the three dimensionless groups Gr_H, Pr and A is determined by conducting a sequence of numerical experiments for different values of Gr_H, Pr and A, and by comparing the resulting flow patterns and temperature fields.

The numerical solution of (49)–(54) was accomplished based on a finite-difference method and the observation that, owing to the symmetry of the problem, only the left half of the flow needs to be calculated. The fluid region of interest was covered with m vertical and n horizontal grid lines; the grid fineness $m = n = 41$ was found to be adequate for the present solution. As shown in figure 4(*b*), rectangular meshes of size $l \times h$ were chosen such that $h/l = A$; consequently, the uppermost grid point on each vertical grid line coincided with the top wall of the enclosure.

Except for the nonlinear terms, all spatial derivatives in the governing differential equations (49)–(53) were approximated at the interior grid points using the central-difference formula (Roache 1976). The successive overrelaxation method (Roache 1976) was employed to find from (51) the stream function for a known vorticity distribution. To solve both (52) and (53) we used a function subprogram (Chow 1979) able to handle an equation of the general form

$$\frac{\partial \phi}{\partial t} = -\frac{\partial (u\phi)}{\partial x} - \frac{\partial (v\phi)}{\partial y} + C\frac{\partial Q}{\partial x} + D\left(\frac{\partial^2 \phi}{\partial x^2} + \frac{\partial^2 \phi}{\partial y^2}\right). \tag{55}$$

The details of this subprogram are omitted here, as they can be found in a textbook-level presentation in Chow (1979).

The effect of fluid motion on the heat transfer between the two walls of the attic was evaluated by computing the Nusselt number

$$Nu = -A \int_{\delta/H}^{A^{-1}} \left(\frac{\partial T}{\partial y}\right)_{y=0} \mathrm{d}x, \tag{56}$$

where δ is the length of the inert (isothermal) region at the left-hand corner of the wedge, as discussed at the end of §3 (figure 1). Equation (56) was integrated numerically for each instant in time. In order to be able to discuss comparatively the evolution of Nu in time and the influence of Gr_H, Pr and A on the heat-transfer rate, δ/L was set equal to 0.1 throughout the present study. Note that for δ/L values much smaller than 0.1 the Nusselt number calculated using (56) would be dominated

by the tip region. We felt that for a meaningful discussion of the convective heat-transfer effect, δ/L should be large enough to remove from the picture the unrealistically large conduction effect through the tip.

It is worth mentioning that in the development of the numerical solution we experimented also with non-uniform grids and advanced differencing methods. These alternative techniques did not improve the solution significantly, in view of the added complications. Most importantly, the use of alternative techniques did not widen the range of Grashof number amenable to a stable numerical solution by the finite-difference method.

6. Results and discussion

6.1. *The effect of Grashof number*

The results of the numerical experiments are shown in figures 5–7. In the case of $Gr_H = 10^5$, which is the highest Grashof number investigated in the present study, we report the evolution and approach to steady state of the temperature, the horizontal velocity and the stream function evaluated at $x = \frac{1}{2}L/H$. The sudden cooling of the top wall initiates a counterclockwise circulation in the enclosure (see figures 5*b*, *c*). The velocities are initially the highest near the roof of the attic, which is the surface driving the flow. At the same time, the body of fluid residing outside the top-wall layer moves slowly to the right in 'uniform-flow' fashion. As time progresses, the entire fluid is slowly entrained in the gyre; the steady state is reached at a dimensionless time $t \approx 0.2$. The manner in which the temperature field approaches the steady state indicates the presence of a sizable convective effect during the early part of the transient experiment (see figure 5*a*). In the steady state, the temperature field departs noticeably from the pure-conduction limit; however, conduction is still the major heat-transfer mechanism. We do not observe any steep temperature gradients near the walls which would indicate the presence of warm and cold fluid jets parallel to the bottom and top walls. In other words, despite the relatively high value of Gr_H, the convective heat-transfer mechanism does no appear to dominate the case documented in figure 5. This conclusion is in agreement with the scaling criterion (38), which, for this case ($Ra_H = 0.72 \times 10^5$, $A = 0.2$), yields $Ra^{\frac{1}{4}}A^{\frac{1}{2}} \approx 7$, which is not appreciably higher than one. The steady-state flow pattern is ruled by the counterclockwise cell shown in figure 5(*d*).

An interesting aspect of these numerical results is that both the horizontal-velocity and stream-function profiles (figures 5*b*, *c*) do not approach the steady state monotonically, but in an oscillatory fashion. The steady state is reached after the oscillation is damped out by viscous diffusion. The oscillatory approach to steady state is a feature present in all numerical experiments considered in this study.

The relative importance of convective heat transfer is illustrated by the Nusselt-number approach to steady state. Figure 6 shows Nu first rising to a peak value (at $t = 0.086$) and subsequently decaying to the steady-state value $Nu = 3.64$ for $t > 0.2$. The increase in the steady-state Nu-value confirms the increased importance of convection as a heat transfer mechanism. The peak in the $Nu(t)$ curve indicates the time of most intense heat transfer between the bottom wall and the attic fluid. This time corresponds to the first sweep made along the bottom wall (warm) by the jet cooled by the top wall. According to §4, the time of this first sweep scales as L/u_{1f}, hence the dimensionless time t corresponding to maximum Nu on figure 6 must scale as

$$t_{Nu_{\max}} \approx A^{-1}Pr^{\frac{1}{2}}Gr_H^{-\frac{1}{2}}. \tag{57}$$

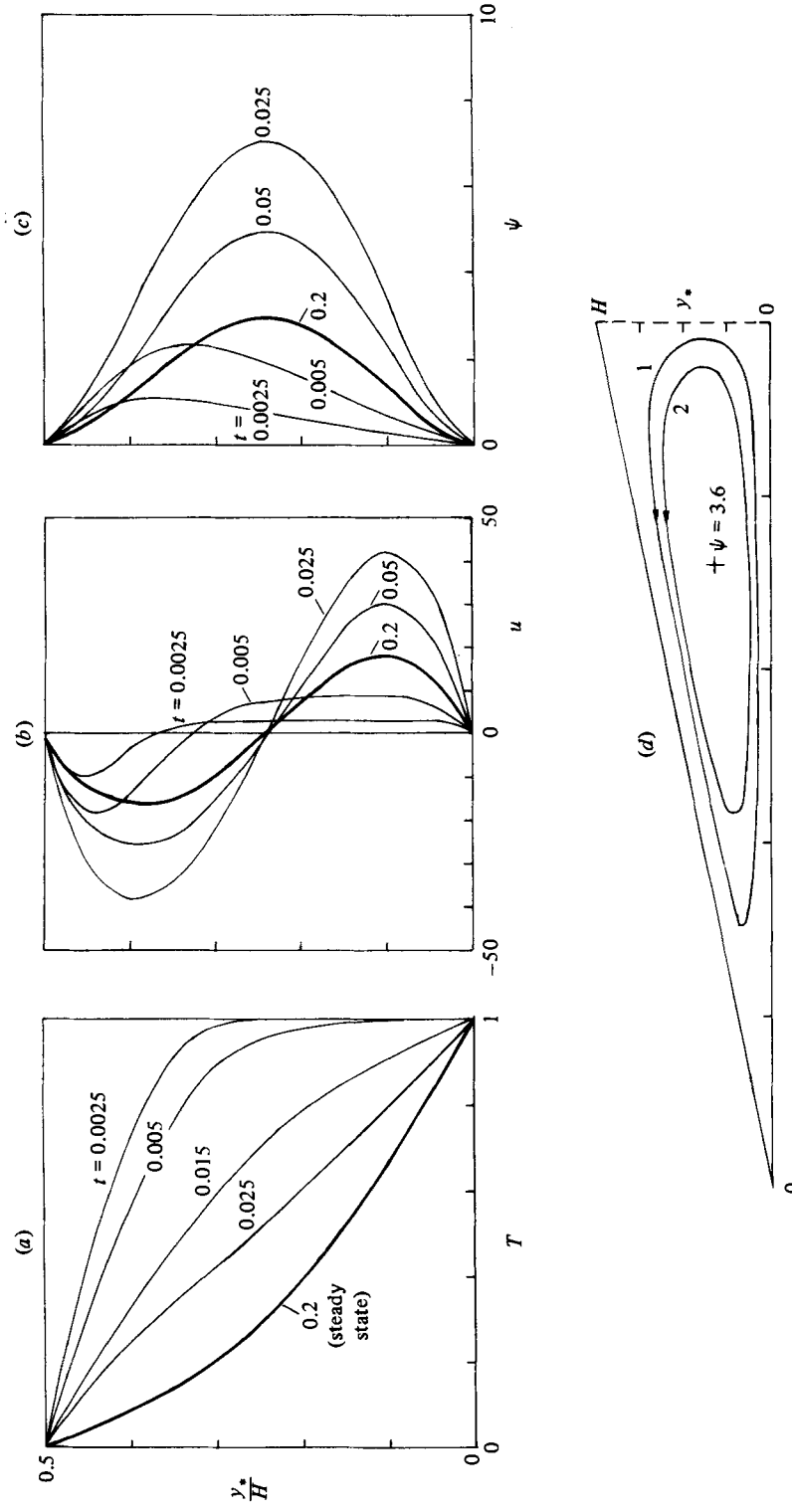

FIGURE 5. Numerical results for $A = 0.2$, $Gr_H = 10^5$, $Pr = 0.72$: (*a*) the temperature profile at $x_* = \frac{1}{2}L$; (*b*) the horizontal-velocity profile at $x_* = \frac{1}{2}L$; (*c*) the stream-function profile at $x_* = \frac{1}{2}L$; (*d*) the steady-state streamline pattern.

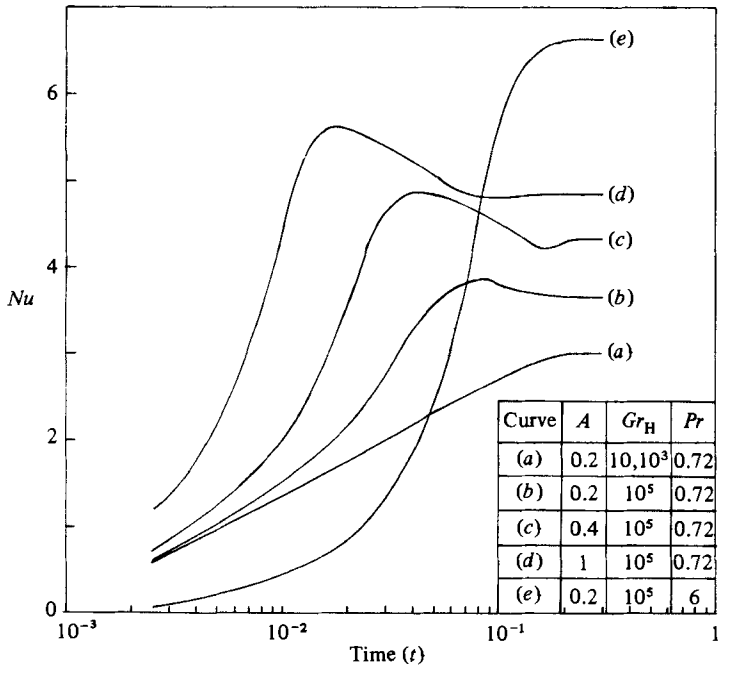

FIGURE 6. The Nusselt-number approach to steady state.

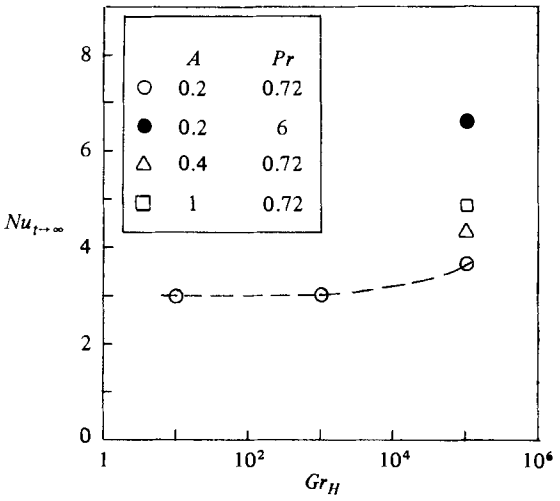

FIGURE 7. The dependence of Nu on Gr_H, A and Pr, in the steady state ($t\to\infty$).

Thus the peak of the $Nu(t)$ curve and the time of approach to the final Nu-value migrate to the left as Gr_H increases (figure 6).

Numerical experiments conducted at lower Grashof numbers ($Gr_H = 10, 10^3$) revealed similar flow characteristics: thus, for the sake of brevity, these experiments are not shown. However, curve (*a*) on figure 6 shows the Nusselt-number variation *vs.* time, and figure 7 shows the special effect of Gr_H on the final heat-transfer rate between the top and bottom walls. Figure 7 shows that below $Gr_H = 10^3$ the Nusselt number is practically independent of Grashof number.

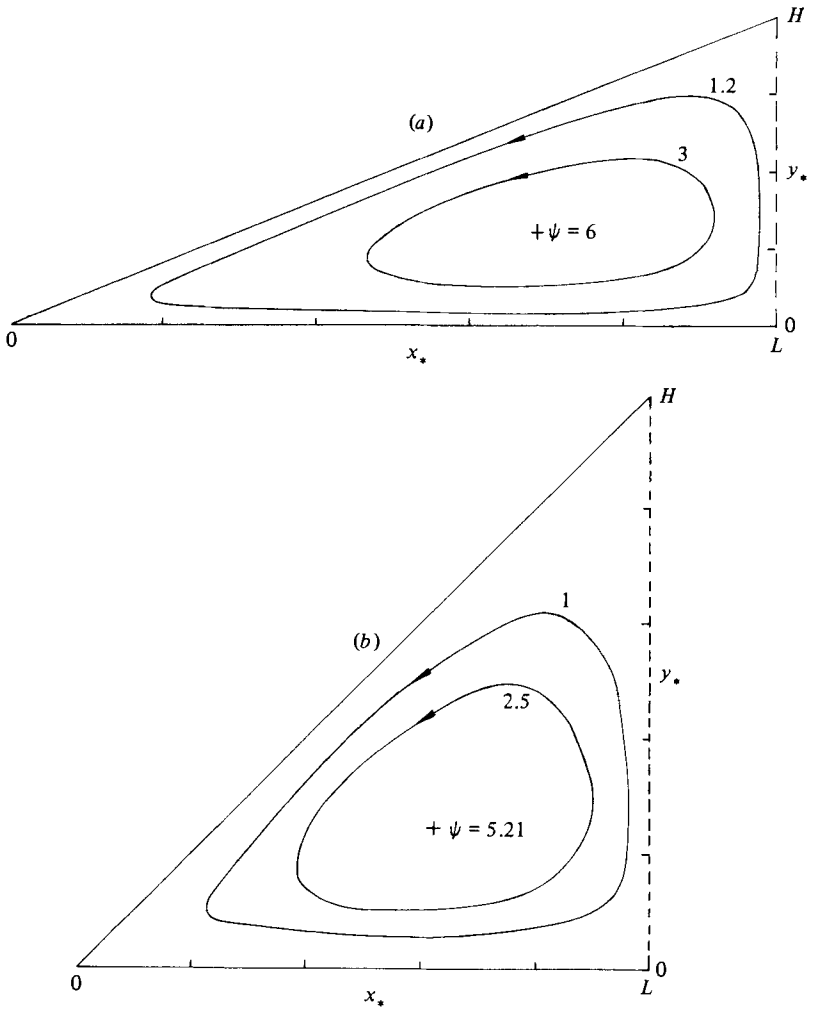

FIGURE 8. Steady-state streamline patterns: (*a*) $A = 0.4$, $Gr_H = 10^5$, $Pr = 0.72$; (*b*) $A = 1$, $Gr_H = 10^5$, $Pr = 0.72$.

6.2. *The effect of aspect ratio, $A = H/L$*

We carried out two additional experiments (figure 8) to determine how seriously the aspect ratio A affects the flow pattern and temperature field in the enclosure. During these experiments the Prandtl number was kept unchanged, $Pr = 0.72$. Expecting that higher aspect ratios A would stimulate the circulation, we assigned to the Grashof number the highest value we were able to simulate stably ($Gr_H = 10^5$). In both experiments the temperature, horizontal-velocity and stream-function variations in the vertical exhibited similar behaviour to the $A = 0.2$ case reported in figures 5(*a–c*). The steady-state streamlines consist, once again, of one counterclockwise cell; however, as expected, the circulation in figure 8 is stronger. According to figure 6, in the case $A = 0.4$ the Nusselt number reaches a peak value at $t = 0.044$, i.e. faster than in a shallower space ($A = 0.2$, $Gr_H = 10^5$) and in agreement with the criterion (57); subsequently Nu reaches a minimum value at $t = 0.17$ and finally approaches monotonically the steady state at $t = 0.19$. The relatively fast decay of the internal wave motion suggests the presence of effective viscous damping. The convective

contribution to heat transfer is enhanced by the increasing A, as indicated by the steady-state value of Nu (figures 5 and 6).

Increasing the aspect ratio to $A = 1.0$ 'speeds up' the duration of the transient phase of the experiment. The internal wave motion and its decay take place earlier and, as shown in figure 5, steady state is reached at $t \approx 0.125$.

Finally, figure 6 summarizes the effect of aspect ratio A on the net heat transfer. It is apparent that the increasing values of A lead to increasingly higher Nusselt numbers: this effect is to be expected from the scaling analysis (criterion (29)), which showed that increasing the numerical value of the dimensionless group $Ra_H^{\frac{1}{4}} A^{\frac{1}{2}}$ enhances the convective contribution to heat transfer, and eventually results in a thermal layering structure in the enclosure.

6.3. *The effect of Prandtl number Pr*

An important dimensionless parameter whose effect remains to be examined is the Prandtl number. We conducted an additional experiment at $Pr = 6$ (water), in a cavity with an aspect ratio and a Grashof number considered earlier, $A = 0.2$, $Gr_H = 10^5$. Figure 6 shows that for $Pr = 6$ the Nusselt number approaches steady state monotonically, indicating a highly effective viscous damping of the internal wave motion. The steady-state value reached by Nu (figure 6) suggests a strong convective contribution to the net heat-transfer rate. Time-dependent velocity and temperature profiles were plotted for this experiment in the same fashion as in figure 5; however, these plots are not shown here owing to space limitations. The temperature profiles showed that the temperature change in the vertical direction takes place in the vicinity of the walls, demonstrating that increasing the Prandtl number leads to a temperature field composed of two thermal boundary layers sandwiching a nearly isothermal core region. The scaling criterion (29) predicts this behaviour, since in the case ($Gr_H = 10^5$, $Pr = 6$, $A = 0.2$) the order of magnitude of $Ra_H^{\frac{1}{4}} A^{\frac{1}{2}}$ is greater than unity.

The flow field is found to exhibit oscillatory behaviour and reaches steady state at $t > 0.25$. We did not observe the presence of viscous layers along the two walls, in agreement with the criterion (34) sine the group $Pr^{-\frac{1}{2}} Ra_H^{\frac{1}{4}} A^{\frac{1}{2}}$ is of order unity. The steady-state streamline pattern revealed that as Pr increases, the streamlines make their 'corner' turn closer to the centre of the attic. The strong effect of Pr on Nu is shown in figure 6, which lists the steady-state values of Nu for $Pr = 0.72$ and $Pr = 6$ for the same $A = 0.2$ and $Gr_H = 10^5$. This effect is explained by the scaling analysis of §4: in the convection-dominated regime, the Nusselt number defined by (56) scales as H/δ_{1f}, in other words

$$Nu \approx A^{\frac{1}{2}} Pr^{\frac{1}{4}} Gr_H^{\frac{1}{4}}. \tag{58}$$

6.4. *The effect of the temperature boundary conditions on the stability of the flow field*

If, in addition to being cooled from the top, the attic fluid is heated from below, it may not reach the elongated single-cell steady state illustrated in figures 5(*d*) and 8. Instead, the attic fluid may experience a local thermal instability of the Bénard type (Bénard 1901; Rayleigh 1916; Chandrasekhar 1961). We conducted an additional experiment to investigate this possibility; however, owing to space limitation we do not show the plotted temperature and flow-field history. In this experiment the $T = 0.5$ isothermal attic was simultaneously heated along the bottom wall ($T = 1$) and cooled along the top wall ($T = 0$). The experiment focused on a cavity filled with air ($Pr = 0.72$) and subjected to conditions that are most favourable to the Bénard instability, namely the highest possible Grashof number (10^5) and a nearly horizontal

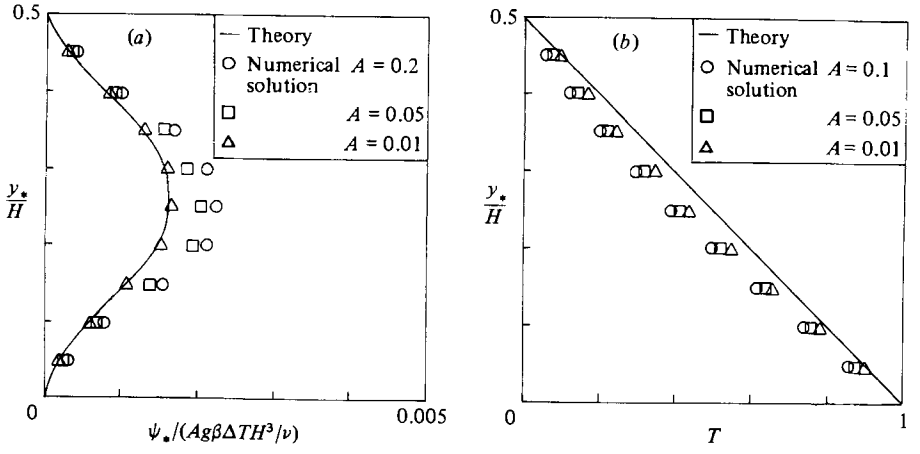

FIGURE 9. Comparison of theoretical and numerical results; $Gr_H = 10^3$, $Pr = 0.72$.

roof $A = 0.2$. The numerical results revealed the fact that the flow is stable throughout its evolution to steady state. Furthermore, the steady-state temperature and flow fields were found to be nearly identical to those reported already in figures 5(*a–d*). It is worth mentioning that the fluid motion is once again initiated in the vicinity of the top wall, because it is the only wall not perpendicular to the direction of gravity.

6.5. *Numerical verification of the asymptotic theory of section* 3

In order to establish the range of validity of the analytical results developed in §3, we conducted a number of numerical calculations for the stream-function and temperature profiles in the vertical plane $x_* = \frac{1}{2}L$ for $Gr_H = 1000$ and a range of aspect ratios A. As shown in figures 9(*a*, *b*), the asymptotic theory predicts the flow and temperature fields adequately, provided that $A \leqslant 0.01$. For the lowest aspect ratio considered in these numerical tests ($A = 0.01$) the theoretical stream function predicts to within 0.03 % the numerical results. The theoretical temperature profile deviates only slightly from the numerical profile (figure 9*b*): this discrepancy stems from the fact that the theoretical curve represents one-dimensional conduction in the vertical direction, whereas the numerical solution accounts also for the minimal conduction effect in the horizontal direction.

This research was supported in part by the National Science Foundation through Grant no. ENG 78-20957.

Appendix

Coefficients c_i, $i = 1, \ldots, 5$, *in* (16):

$$\left.\begin{aligned} c_1 &= \frac{Gr_H Pr}{5040}\frac{3f'^2+ff''}{f^4}, \quad c_2 = -\frac{Gr_H Pr}{800}\frac{3f'^2+ff''}{f^2}, \\ c_3 &= \frac{Gr_H Pr}{720}\frac{3f'^2+ff''}{f}, \quad c_4 = -\frac{1}{6}\frac{ff''-2f'^2}{f^3}, \\ c_5 &= -\left\{\frac{1224Gr_H Pr}{3628800}(3f'^2+ff'') - \frac{1}{6}\frac{ff''-2f'^2}{f}\right\}. \end{aligned}\right\} \tag{A 1}$$

Coefficients $a_i, i = 1, \ldots, 9$, *in* (17):

$$\left.\begin{aligned}
a_1 &= \frac{1}{7920}\left(\frac{Gr_H}{360}\frac{ff'f''-2f'^3}{f^5}+c_1'\right),\\
a_2 &= \frac{1}{3024}\left[Gr_H\left(-\frac{1}{200}\frac{f'f''}{f^2}+0.0225\frac{f'^3}{f^3}\right)+c_2'\right],\\
a_3 &= \frac{1}{1680}\left(-\frac{Gr_H}{720}\frac{13f'^3+ff'f''}{f^2}+c_3'\right),\\
a_4 &= \frac{1}{840}\left(\frac{3Gr_H}{400}f'f''-\frac{1}{3}\frac{f^2f''-6ff'f''+6f'^3}{f^4}+c_4'\right)\\
a_5 &= -\frac{Gr_H}{72000}ff'f'',\\
a_6 &= \frac{1}{120}\left\{\frac{Gr_H}{900}(ff'^3+f^2f'f'')+\frac{3}{10}f'''+c_5'\right\},\\
a_7 &= -\frac{1}{360}(3f'f''+ff'''),\\
a_8 &= -(9a_1f^8+7a_2f^6+6a_3f^5+5a_4f^4+4a_5f^3+3a_6f^2+2a_7f),\\
a_9 &= -(a_1f^9+a_2f^7+a_3f^6+a_4f^5+a_5f^4+a_6f^3+a_7f^2+a_8f).
\end{aligned}\right\} \quad \text{(A 2)}$$

In the above expressions the primes denote differentiation with respect to x.

Coefficients $c_i, i = 1, \ldots, 5$, *in* (16) *for* $f(x) = x$:

$$\left.\begin{aligned}
c_1 &= \frac{Gr_H Pr}{1680}\frac{1}{x^4}, \quad c_2 = -\frac{3Gr_H Pr}{800}\frac{1}{x^2}, \quad c_3 = \frac{Gr_H Pr}{240}\frac{1}{x},\\
c_4 &= \frac{1}{3}\frac{1}{x^3}, \quad c_5 = -\left(\frac{17Gr_H Pr}{16\,800}x^2+\frac{1}{3}\frac{1}{x}\right).
\end{aligned}\right\} \quad \text{(A 3)}$$

Coefficients $a_i, i = 1, \ldots, 9$, *in* (17) *for* $f(x) = x$:

$$\left.\begin{aligned}
a_1 &= -\frac{Gr_H}{7920}\left(\frac{1}{180}+\frac{Pr}{420}\right)\frac{1}{x^5}, \quad a_2 = \frac{Gr_H}{3024}\left(0.0225+\frac{3Pr}{400}\right)\frac{1}{x^3},\\
a_3 &= -\frac{Gr_H}{1680}\left(\frac{117}{6480}+\frac{Pr}{60}\right)\frac{1}{x^2}, \quad a_4 = -\frac{1}{280}\frac{1}{x^4}, \quad a_5 = 0,\\
a_6 &= \frac{1}{120}\left\{Gr_H\left(\frac{1}{900}-\frac{17Pr}{8400}\right)x+\frac{1}{3}\frac{1}{x^2}\right\}, \quad a_7 = 0,\\
a_8 &= -(9a_1x^8+7a_2x^6+6a_3x^5+5a_4x^4+3a_6x^2),\\
a_9 &= 8a_1x^9+6a_2x^7+5a_3x^6+4a_4x^5+2a_6x^3.
\end{aligned}\right\} \quad \text{(A 4)}$$

REFERENCES

Arpaci, V. S. 1966 *Conduction Heat Transfer*, pp. 180–248. Addison-Wesley.

Bejan, A. & Poulikakos, D. 1982 Natural convection in an attic shaped space filled with porous material. *Trans. ASME* C: *J. Heat Transfer* **104**, 241–247.

Bénard, H. 1901 Les Tourbillons cellulaires dans une nappe liquide transportant de la chaleur par convection en régime permanent. *Ann. Chim. et Phys.* **23**, 62–144.

CATTON, I. 1979 Natural convection in enclosures. *Keynote paper, 6th Intl Heat Transfer Conf., Toronto* 1978, vol. 6, pp. 13–43.

CHANDRASEKHAR, S. 1961 *Hydrodynamic and Hydromagnetic Stability*, pp. 9–75. Oxford University Press.

CHOW, C. Y. 1979 *An Introduction to Computational Fluid Mechanics*. Wiley.

CORMACK, D. E., LEAL, L. G. & IMBERGER, J. 1974 Natural convection in a shallow cavity with differentially heated end walls. Part 1. Asymptotic theory. *J. Fluid Mech.* **65**, 209–230.

FLACK, R. D. 1980 The experimental measurement of natural convection heat transfer in triangular enclosures heated or cooled from below. *Trans. ASME* C: *Transfer* **102**, 770–772.

FLACK, L. D., KONOPNICKI, T. T. & ROOKE, J. H. 1979 The measurement of natural convective heat transfer in triangular enclosures. *Trans. ASME* C: *J. Heat Transfer* **101**, 648–654.

OSTRACH, S. 1972 Natural convection in enclosures. *Adv. Heat Transfer* **8**, 161–227.

PATTERSON, J. & IMBERGER, J. 1980 Unsteady natural convection in a rectangular cavity. *J. Fluid Mech.* **100**, 65–86.

RAYLEIGH, LORD 1916 On convective currents in a horizontal layer of fluid when the higher temperature of fluid is on the underside. *Phil. Mag.* **32**, 529–546.

ROACHE, P. J. 1976 *Computational Fluid Dynamics*. Hermosa.

WALKER, K. L. & HOMSY, G. M. 1978 Convection in a porous cavity. *J. Fluid Mech.* **87**, 449–474.